

Principal dynamic mode analysis of action potential firing in a spider mechanoreceptor

Georgios D. Mitsis · Andrew S. French ·
Ulli Höger · Spiros Courellis · Vasilis Z. Marmarelis

Received: 20 July 2005 / Accepted: 1 August 2006 / Published online: 5 October 2006
© Springer-Verlag 2006

Abstract The encoding of mechanical stimuli into action potentials in two types of spider mechanoreceptor neurons is modeled by use of the principal dynamic modes (PDM) methodology. The PDM model is equivalent to the general Wiener–Bose model and consists of a minimum set of linear dynamic filters (PDMs), followed by a multivariate static nonlinearity and a threshold function. The PDMs are obtained by performing eigen-decomposition of a matrix constructed using the first-order and second-order Volterra kernels of the system, which are estimated by means of the Laguerre expansion technique, utilizing measurements of pseudorandom mechanical stimulation (input signal) and the resulting action potentials (output signal). The static nonlinearity, which can be viewed as a measure of the probability of action potential firing as a function of the PDM output values, is computed as the locus of points of the latter that correspond to output action potentials. The performance of the model is assessed by computing receiver operating characteristic (ROC) curves, akin to the ones used in decision theory and quantified by computing the area under the ROC curve. Three PDMs are revealed by the analysis. The first PDM exhibits a

high-pass characteristic, illustrating the importance of the velocity of slit displacement in the generation of action potentials at the mechanoreceptor output, while the second and third PDMs exhibit band-pass and low-pass characteristics, respectively. The corresponding three-input nonlinearity exhibits asymmetric behavior with respect to its arguments, suggesting directional dependence of the mechanoreceptor response on the mechanical stimulation and the PDM outputs, in agreement to our findings from a previous study (Ann Biomed Eng 27:391–402, 1999). Differences between the Type A and B neurons are observed in the zeroth-order Volterra kernels (related to the average firing), as well as in the magnitudes of the second and third PDMs that perform band-pass and low-pass processing of the input signal, respectively.

1 Introduction

Mechanoreceptors perform the detection and transduction of mechanical stimuli in many types of animal tissue, providing many inputs to the central nervous system. In addition to sensory functions, such as hearing, touch and balance, mechanoreceptors are involved in regulatory mechanisms in the cardiovascular, respiratory and renal systems. Mechanotransduction usually involves at least three stages of signal processing: mechanical coupling of the stimulus to the sensory cell membrane, transduction of the membrane deformation into a receptor current, and encoding of the receptor current into action potentials (French 1992). In order to accommodate a broad range of naturally occurring stimuli, mechanoreceptors are characterized by adaptive properties with respect to gain and operating range and they can subsequently

G. D. Mitsis · S. Courellis · V. Z. Marmarelis
Department of Biomedical Engineering,
University of Southern California, Los Angeles,
CA 90089, USA

A. S. French · U. Höger
Department of Physiology and Biophysics,
Dalhousie University, Halifax NS B3H 1X5, Canada

G. D. Mitsis (✉)
FMRIB Centre, University of Oxford,
John Radcliffe Hospital, Headington,
Oxford OX3 9DU, UK
e-mail: gmitsis@fmrib.ox.ac.uk

exhibit a wide range of firing patterns that are matched to their functions.

The extraction of mathematical/computational models that can accurately predict the responses of mechanoreceptors to a wide range of physiological stimuli can lead to a better understanding of the underlying physiology and the way in which the central nervous system receives information from internal and external mechanical events. They also allow the construction of larger scale models that involve mechanoreceptor feedback. However, the dynamic behavior of mechanoreceptors is not yet fully understood due to their small physical size and limited accessibility, as well as their complex and nonlinear characteristics. In previous modeling studies of mechanoreceptor function, linear techniques such as transfer function analysis have been employed (French et al. 1972; Koles and Smith 1974; Looft and Baltensperger 1990; Matthews and Stein 1969). In Del Prete et al. [2003] multiple logistic regression models that included first-order interactions were employed to study mouse skin mechanoreceptors. More recently, nonlinear Volterra–Wiener models have been utilized to describe the function of insect mechanoreceptors (French and Korenberg 1989; French and Patrick 1994; French and Marmarelis 1995; French et al. 2001; Marmarelis et al. 1999), crab proprioceptors (DiCaprio 2003; Gamble and DiCaprio 2003), locust proprioceptors (Kondoh et al. 1995), as well as the encoding of tactile stimuli in the barrel cortex of mice (Webber and Stanley 2004). The aforementioned have included both models that incorporated prior electrophysiological knowledge about specific receptors (e.g., French and Patrick 1994) and “black-box” models that did not assume any prior knowledge about structural characteristics (e.g., Marmarelis et al. 1999; Gamble and DiCaprio 2003).

In the present study we model the dynamic transduction of mechanical stimuli into action potentials in two types of mechanoreceptor neurons from a spider lyriform organ that are morphologically similar but exhibit different dynamic characteristics. Type A neurons are rapidly adapting and produce only one or two action potentials in response to step electrical or mechanical stimuli, while Type B neurons adapt more slowly and produce a burst of many action potentials with similar stimuli (Seyfarth and French 1994).

For this purpose, we employ the principal dynamic mode (PDM) methodology for spike-output systems (Marmarelis 1997, 2004; Marmarelis and Orme 1993). The PDM method is based on the general Wiener–Bose model (Bose 1956) and aims to extract the most significant dynamic components of a nonlinear system in the form of a minimum set of linear filters that process

the input, after estimating its first and second-order Volterra kernels (Marmarelis 1997). The PDM outputs feed a multiple-input static nonlinearity and a subsequent threshold function to yield the output action potentials. We present herein the obtained PDM models for both neuron types in order to examine whether the aforementioned differences between them are reflected in the form of the dynamics estimated from pseudo-random mechanical stimulation. This study extends our previous findings employing the PDM methodology to model the dynamics of the conversion of mechanical displacements into transmembrane receptor current and potential in a spider mechanoreceptor (Marmarelis et al. 1999).

2 Methods

2.1 Animals and preparations

Animal protocols were approved by the Dalhousie University Committee on Laboratory Animals. Adult spiders, *Cupiennius salei*, of either sex were taken from a laboratory colony. The preparation for mechanical stimulation of the sensory neurons has been described before (Seyfarth and French 1994; Juusola et al. 1995). A concave piece of cuticle containing the intact VS-3 lyriform organ, was dissected from the patella of an autotomized leg and mounted on a custom designed holder. The neurons were visually identified under a dissecting microscope and penetrated with microelectrodes from above. Dissection and all experiments were performed in spider saline (Sekizawa et al. 1999: 223 mM NaCl, 6.8 mM KCl, 8 mM CaCl₂, 5.1 mM MgCl₂, 10 mM HEPES, pH 7.8). All chemicals were obtained from SIGMA (Oakville, ON).

2.2 Recording and stimulation

The discontinuous (switching) single electrode current-clamp technique (Finkel and Redman 1984) was used to record cell membrane potentials with a SEC-10L amplifier (NPI Electronic, Tamm, Germany). Borosilicate glass microelectrodes were pulled by a horizontal puller (P2000, Sutter Instrument Co., Novato, CA, USA), filled with 3 M KCl, and coated with petroleum jelly to decrease stray capacitance (Juusola et al. 1997). The electrode resistances were 45–70 M Ω with time constants of 1–3 μ s in spider saline. Switching frequencies of 20–23 kHz were used with a duty cycle of 1:8 for current passing/voltage recording.

For mechanical stimulation, a piezoelectric stimulator with position control feedback (LVPZ translator, PZT controller; Polytec Physik-Instrumente, Waldbronn, Germany) was mounted on a three-dimensional micro-manipulator that could position the tip of the stimulator probe (diameter $\sim 50 \mu\text{m}$) beneath the outer surface of the VS-3 slits. For electrical stimulation, current was injected directly via the amplifier. The experimental arrangement was mounted on gas-driven vibration isolation table (Technical Manufacturing, Peabody, MA, USA).

Pseudorandom Gaussian white noise was generated by a digital computer via a 33-bit binary sequence algorithm and a 12-bit digital-to-analog converter, and filtered by a nine-pole active filter so that the power spectrum was below 1% of its low frequency asymptote at frequencies above 300 Hz. This cutoff frequency was based on the experimental limitations imposed by the combination of the microelectrode amplifier, the switching current clamp technique and the membrane time constant. Mechanical displacement was sensed by the position transducer in the piezoelectric stimulator, which had a low-pass characteristics with a corner frequency of ~ 80 Hz. Electric current stimuli were recorded directly from the amplifier current output. Membrane potentials, including action potentials, were recorded from the amplifier. Each signal was sampled at 50 kHz by an independent 12-bit analog-to-digital converter to avoid sampling delays between channels. The duration of each recording was approximately 80 s.

2.3 Data pre-processing

Action potentials were separated from the underlying continuous membrane potentials by an algorithm that identified action potentials as the potential increasing and then decreasing by a fixed amplitude within less than 2 ms. The fixed amplitude was in the range between 15 and 20 mV. All separations were inspected visually, together with the original recording, to ensure that the algorithm functioned properly. Separated action potentials were stored as times of occurrence, while the gap caused by action potential separation was filled by linear interpolation. Action potential signals were digitally filtered by convolution with the $\sin(x)/x$ function to band-limit them to the range 0–500 Hz and produce a regularly sampled (1 ms interval) signal. This filter characteristic was chosen because it has a flat frequency response, avoids additional filtering of the sampled analog input signal and can be easily and efficiently implemented (French and Holden 1971). Sampled analog signals of mechanical displacement were digitally re-sampled by averaging to give a 1 ms sample interval.

2.4 Model estimation

The general Wiener–Bose model of a nonlinear system (Bose 1956) is shown in Fig. 1. The discrete-time input signal $x(n)$ is convolved with the linear filters $\{L_1, L_2, \dots, L_K\}$, i.e.:

$$u_i(n) = \sum_{m=0}^{M_i} l_i(m)x(n - m), \quad i = 1, 2, \dots, K, \quad (1)$$

where $\{l_1(m), l_2(m), \dots, l_K(m)\}$ are the impulse responses of these filters and M is the system memory. The linear filter outputs are then fed into a multiple-input static nonlinearity, the output of which is given by

$$v(n) = f[u_1(n), u_2(n), \dots, u_K(n)]. \quad (2)$$

In the case of a binary model output, the latter is computed by comparing the static nonlinearity output to a threshold p :

$$y(n) = \begin{cases} 1 & \text{if } v(n) - p > 0, \\ 0 & \text{if } v(n) - p \leq 0. \end{cases} \quad (3)$$

The linear filter impulse responses $\{l_i(m)\}$ are selected from an appropriate basis (e.g., the Laguerre basis) and the static nonlinearity f is estimated from the input–output data. The PDM methodology (Marmarelis and Orme 1993; Marmarelis 1997) aims at extracting a minimum set of linear filters that remain functionally equivalent to the Wiener–Bose model of Fig. 1, which constitute the PDMs of the system. This leads to compact representations that facilitate model interpretation, which is important in the case of physiological systems, as in the present study.

The PDMs can be extracted from the estimates of the Volterra kernels of the system, as indicated below. The general discrete-time Volterra model for a finite-memory, Q th order nonlinear system is

$$y(n) = \sum_{q=0}^Q \left\{ \sum_{m_1} \dots \sum_{m_q} k_q(m_1, \dots, m_q) x(n - m_1) \dots x(n - m_q) \right\}, \quad (4)$$

where $k_q(m_1, \dots, m_q)$ are the linear ($q = 1$) and nonlinear ($q > 1$) Volterra kernels of the system, which describe the linear and nonlinear dynamic effects of the input on the output, respectively. A practical way to estimate the kernels by employing stimulus-response data (in our case, mechanical displacements and the resulting action potentials) data is the Laguerre expansion technique (Marmarelis 1993), which expands the kernels in terms of the discrete-time Laguerre orthonormal basis and uses least-squares fitting to estimate the expansion

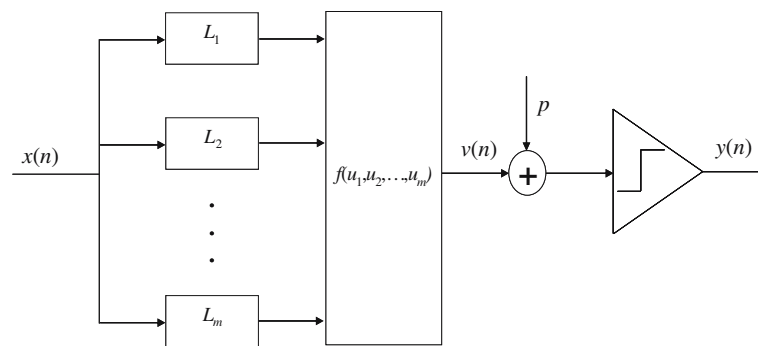


Fig. 1 Principal Dynamic Mode (PDM) model of action potential firing in a spider mechanoreceptor. The PDM model is equivalent to the Wiener–Bose model with a minimum set of linear filters L_1, L_2, \dots, L_m . The input signal (mechanical displacement) is fed

into the PDMs of the system, the outputs of which are combined into a multiple-input static nonlinearity and threshold function to produce the model output

coefficients. One way to estimate the PDMs from the first and second-order kernel estimates is to construct the matrix (Marmarelis 1997):

$$\mathbf{R} = \begin{bmatrix} k_0 & \frac{1}{2}\mathbf{k}_1^T \\ \frac{1}{2}\mathbf{k}_1 & \mathbf{k}_2 \end{bmatrix} \quad (5)$$

which has a size of $(M + 2) \times (M + 2)$, where M is the kernel memory and $k_0, \mathbf{k}_1, \mathbf{k}_2$ are the zeroth, first and second-order Volterra kernels, respectively. \mathbf{R} is real symmetric, therefore its eigenvalues are always real. Note that in this case \mathbf{k}_1 and the eigenvectors of \mathbf{k}_2 were found to be linearly dependent, therefore we were able to reduce \mathbf{R} to \mathbf{k}_2 . By selecting the most important eigenvalues λ_i of \mathbf{R} on the basis of their magnitude, the corresponding orthonormal eigenvectors μ_i define the PDMs of the system, i.e., the impulse responses of the minimum set of linear filters of Fig. 1 (Marmarelis 1997, 2004; Marmarelis and Orme 1993). The number of significant eigenvalues determines the number of the PDMs sufficient to describe the system dynamics. Estimates of higher order kernels can be used for this purpose as well, using singular-value decomposition (Marmarelis 2004). However, this was not found necessary in this application.

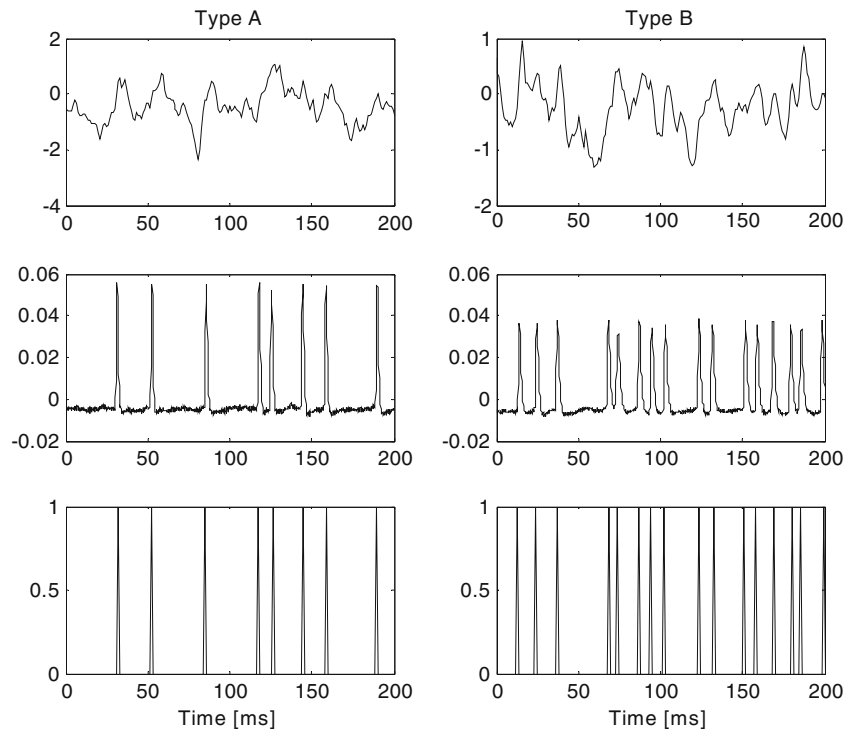
The multivariate static nonlinearity $f(u_1, u_2, \dots, u_K)$ is defined as the locus of points (u_1, u_2, \dots, u_K) that correspond to output action potentials. Therefore, f was constructed by first convolving the input with the PDMs, separating the space of the PDM outputs (u_1, u_2, \dots, u_K) into K -dimensional bins, counting the number of points corresponding to output action potentials and dividing this number by the total number of points within each bin. To account for the 5 ms refractory period between the firing of two consecutive action potentials, we excluded the corresponding points (i.e., they were not counted towards the number of total points). Thus,

$f(u_1, u_2, \dots, u_K)$ yields a measure of the probability of action potential firing as a function of the PDM outputs.

The PDM model performance (in terms of predicting output action potentials correctly) is assessed by constructing receiver operating characteristic (ROC) curves. ROC curves were initially introduced in signal detection theory (Egan 1975) and have been employed also in medical decision applications (McFall and Treat 1999; Swets and Pickett 1992) as well as in a similar context to the present paper (Del Prete et al. 2003). In our case, ROC curves are plots of the true positive fraction as a function of the false positive fraction achieved by the PDM model for all output threshold p values between 0 and 1. The true positive fraction is defined as the number of predicted true positives divided by the total number of true output action potentials for a specific p value and the false positive fraction is defined as the number of predicted false positives divided by the number of maximum possible false positives. Therefore, the ROC curves were constructed by computing the binary output predicted by the PDM model for all values of threshold p between 0 and 1, counting the number of true and false positives by comparing the number and location of the predicted action potentials to those of their true counterparts and calculating the corresponding fractions. The 5 ms refractory period was taken into account in the predicted PDM output by not allowing consecutive action potentials in the model output within this period. For the same reason, predicted action potentials within ± 2 ms of true output action potentials were considered true positives. Finally, as a measure of the model performance, we computed the area under the ROC curve, which lies between 0 and 1. Area values that are closer to 1 denote better performance.

Of the approximately 80,000 data points (sampled at 1 kHz) that were available for each of the four different neurons, segments of 5,000 points (corresponding to

Fig. 2 Representative data segments utilized for model estimation for Type A and Type B neurons. *Top panels* pseudorandom mechanical stimulation (in μm), *middle panels* output action potentials (raw data), *bottom panels* output action potentials (binary data)



150–250 output action potentials) were used to estimate the Volterra kernels and PDMs of the system. Larger sample sizes were found to yield similar kernel estimates. Therefore, 5,000 data points (5 s) were deemed adequate for estimation purposes. The remaining data points were employed to construct the static nonlinearity by mapping the PDM output values onto the output action potentials (60,000 points) and for model validation (15,000 points). For comparison purposes and in order to further quantify the neuron properties for encoding different stimulus parameters, we also performed multiple linear least squares regression analysis on the data segments used to estimate the Volterra kernels, using displacement, displacement velocity as well as displacement acceleration as inputs (regressors) and the resulting action potentials as the output of the regression model. Estimates of velocity and acceleration at each time point were obtained by employing a simple central difference rule.

3 Results

Data from four neurons (2 Type A and 2 Type B) were used for the analysis. Representative segments (length 200 ms) of the stimulus–response waveforms employed to estimate the PDM model are shown in Fig. 2 for both types of neurons. The random mechanical stimulation is shown along with the resulting output action potentials,

in both the raw and processed (binary) waveforms. Type B neurons tended to fire more action potentials under pseudorandom stimulation, even though the stimulus variability was larger for the Type A neurons. The numbers of action potentials during the 80 s recordings were 3,462 and 2,205 for the Type B neurons (with stimulus standard deviations of 0.38 and 0.39 μm , respectively), compared to 1,463 and 2,375 for the Type A neurons (stimulus standard deviations: 1.05 and 0.59 μm). The reason for the discrepancies in stimulus power is that the latter was optimally tuned to each neuron, due to the difficulty in aligning the stimulator with the slit.

The zeroth-order Volterra kernel values (the constant term of the model related to the average firing rate) are given in Table 1 for the Type A and B neurons, averaged over ten different data segments with a length of 5,000 points (i.e., 5 s) from each neuron. The values of k_0 were considerably larger for the Type B neurons. The first-order Volterra kernels for one Type A and one Type B neuron, averaged over ten different data segments, are shown in Fig. 3 in the time and frequency

Table 1 Estimated zeroth-order Volterra kernels for Type A and B neurons, averaged over ten 5 s data segments

	Type A		Type B	
	Neuron 1	Neuron 2	Neuron 1	Neuron 2
k_0	0.018 ± 0.001	0.004 ± 0.001	0.031 ± 0.004	0.038 ± 0.004

Values are mean \pm SE

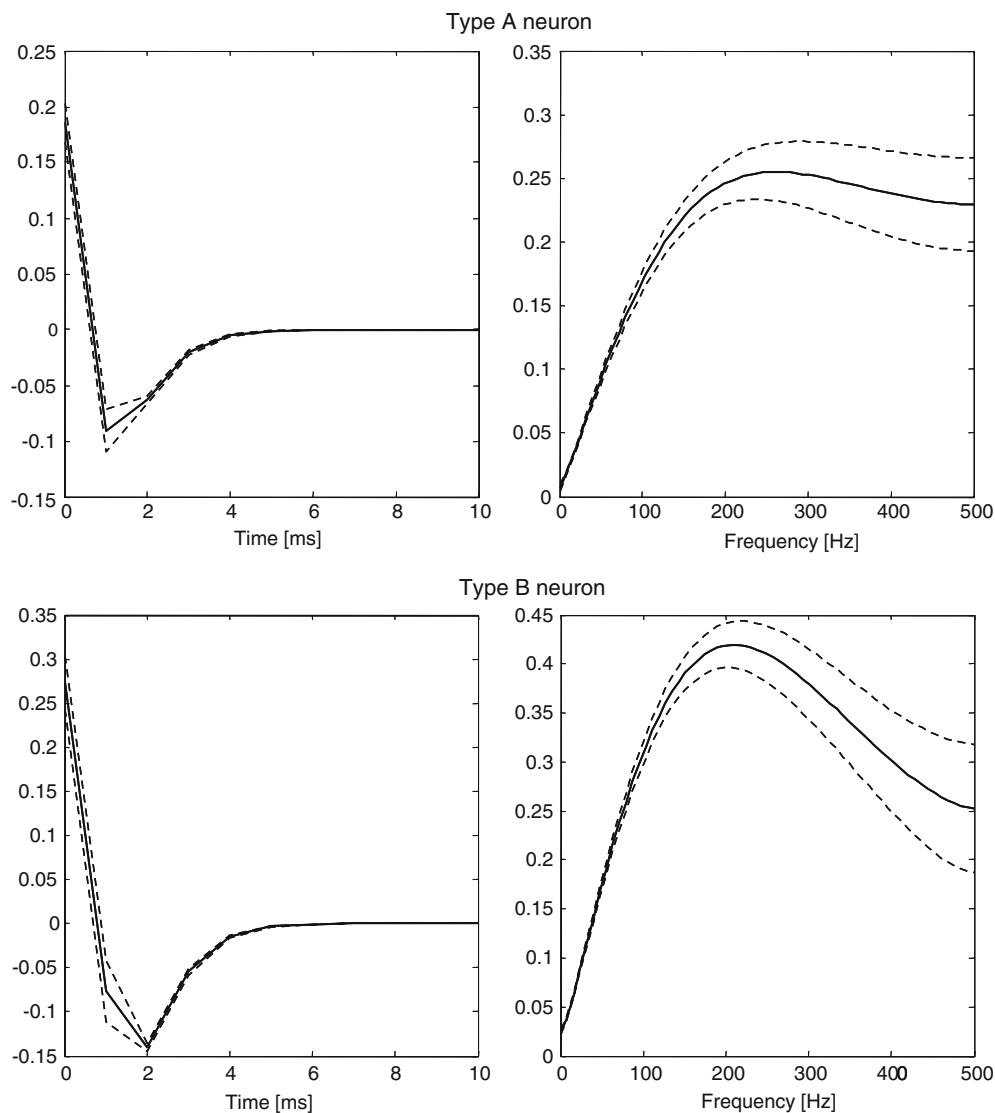


Fig. 3 First-order kernels for one Type A and one Type B neuron in the time and frequency (FFT magnitude) domains, averaged over ten data segments with a length of 5 s. *Solid line* mean, *Dotted line* SE. Note the high-pass characteristic in the frequency domain

(fast fourier transform (FFT) magnitude) domains. The first-order kernels were consistent among different data segments, as shown by the tight error bounds, and exhibit fast dynamics (memory of 6–7 ms) as well as a high-pass characteristic with a frequency peak at around 200 Hz, implying that the linear dynamics depend mostly on the slit displacement velocity. Nonetheless, the fact that the negative undershoot was smaller in magnitude than the initial positive peak indicates that the first-order (linear) dynamics respond to the displacement magnitude as well (in addition to the displacement velocity). The first-order kernels were also found to be similar between the two neuron types, with the Type B neurons exhibiting a slightly larger resonance around 200 Hz. The estimated second-order Volterra kernels for the

two neuron types are shown in Fig. 4 in the two-dimensional time and frequency domains (two-dimensional FFT magnitude). They also exhibit a high-pass characteristic (like their first-order counterparts) and were generally similar for the two neuron types. However, higher magnitude values were observed for the Type B neuron below [200 Hz, 200 Hz] in the two-dimensional frequency plane—a fact that may have important effects on the respective nonlinear responses, since the input power was primarily below 200 Hz.

The improvement achieved in predicting the output waveform by employing nonlinear models is illustrated in Fig. 5 for a representative 200 ms data segment from a Type B neuron. The model prediction achieved by a linear model (blue) is shown along with the prediction

Fig. 4 Second-order kernels for one Type A and one Type B neuron in the time and two-dimensional frequency domains (i.e., magnitude of two-dimensional FFT), averaged over ten data segments with a length of 5 s. Note that the Type B second-order kernel exhibits more power below [200 Hz, 200 Hz] in the bi-frequency plane

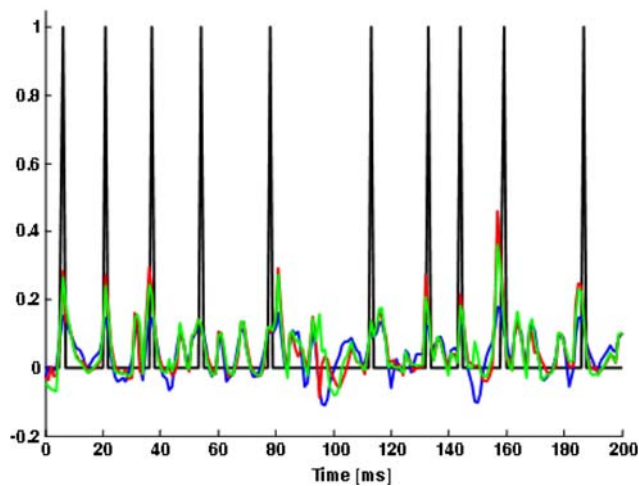
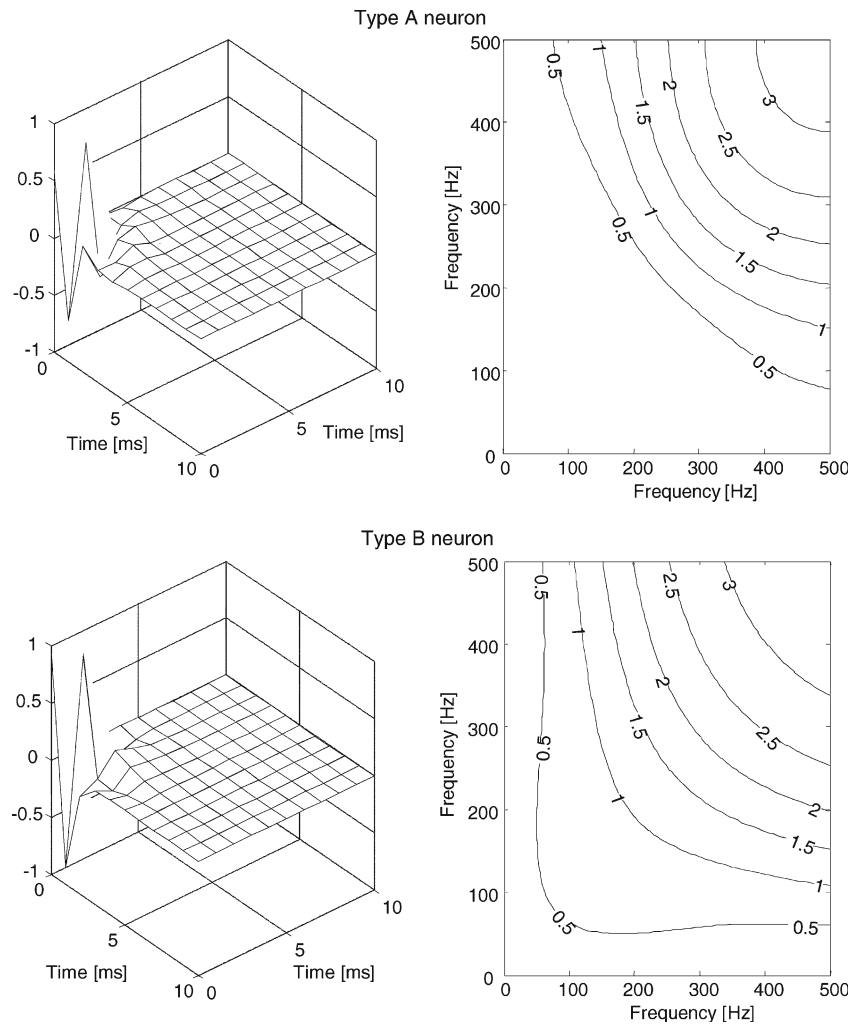


Fig. 5 Representative output prediction achieved by linear and nonlinear Volterra models for a 200 ms segment taken from a Type B neuron. *Blue* linear model prediction, *green* second-order model prediction, *red* third-order model prediction. Note the significant improvement achieved by the nonlinear models

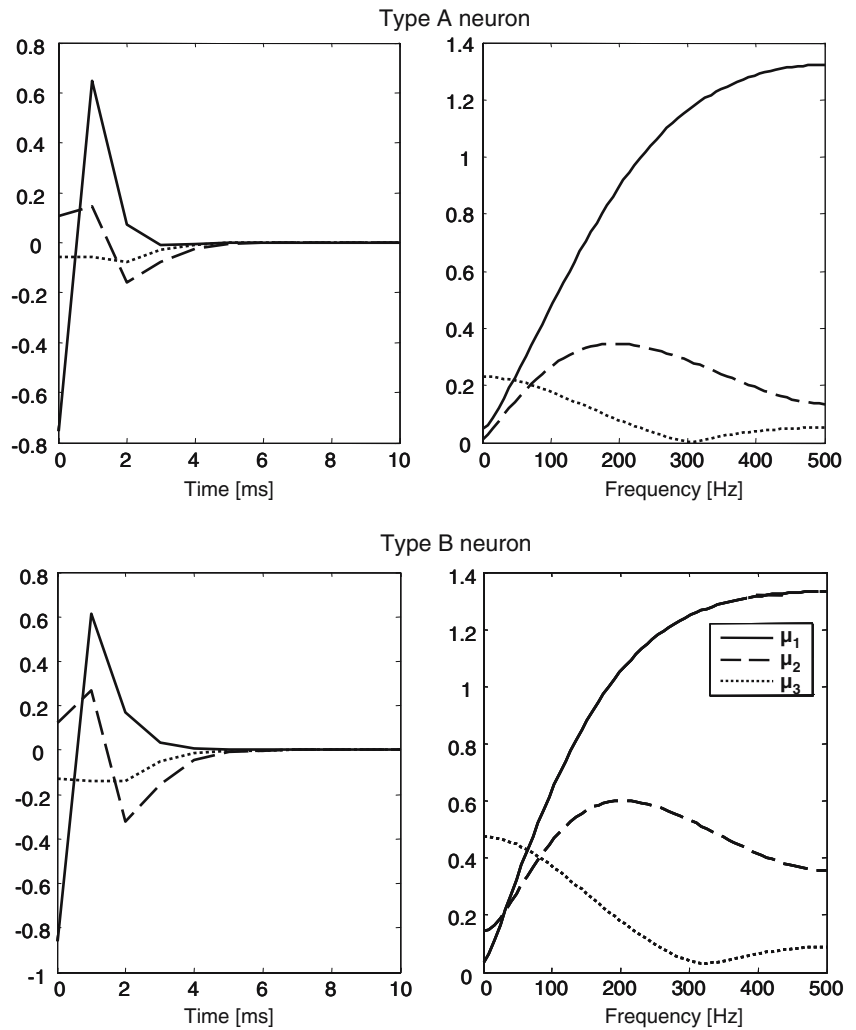
achieved by second and third-order models (green and red, respectively). The inclusion of nonlinear terms improved the model performance considerably, both in terms of predicting the output action potentials and capturing the rectifying characteristic of the output signal (note the areas between action potentials). The normalized mean square error (NMSE), defined as the sum of squares of the model prediction residuals divided

Table 2 Magnitude of the three significant eigenvalues for Type A and B neurons, averaged over ten 5 s data segments

	Type A		Type B	
	Neuron 1	Neuron 2	Neuron 1	Neuron 2
λ_1	0.364 ± 0.015	0.928 ± 0.067	1.721 ± 0.204	1.310 ± 0.205
λ_2	0.024 ± 0.004	0.076 ± 0.009	0.301 ± 0.028	0.134 ± 0.028
λ_3	0.003 ± 0.001	0.015 ± 0.001	0.053 ± 0.006	0.020 ± 0.004

Values are mean \pm SE

Fig. 6 Representative PDMs, scaled by the square root of the corresponding eigenvalue, obtained from the binary output waveforms (see Fig. 2) for one Type A and one Type B neuron in the time and frequency domains. The first, second and third PDM exhibits high-pass, band-pass and low-pass characteristics, respectively. Note that the magnitudes of the second and third PDMs are larger for the Type B neuron



by the sum of squares of the true output, is high due to the binary nature of the output signal (around 90% for linear models and 75–80% for nonlinear models). Third-order models reduced the prediction NMSE by around 5% compared to second-order models. This is also observed in Fig. 5, where the third-order terms build on the second-order model prediction without introducing new spike locations. However, the performance of second and third-order models after the calculation of the static nonlinearity, as assessed by the area under the ROC curve, was found to be comparable (see below).

Eigen decomposition of the matrix \mathbf{R} given by Eq. (5) revealed three significant eigenvalues, the corresponding eigenvectors of which yielded the three PDMs μ_1 , μ_2 and μ_3 . The magnitude of the eigenvalues is given in Table 2 for all four neurons, averaged over the ten 5 s data segments. Type B neurons were characterized by larger eigenvalue magnitudes. Representative PDMs are shown in Fig. 6 in the time and frequency domains for the two neurons of Figs. 3, 4, after scaling by the

square root of the corresponding eigenvalue. The first (most significant) PDM has a high-pass (differentiating) characteristic, suggesting that its output depends primarily on the slit displacement velocity and secondarily on the displacement magnitude. The second PDM has a band-pass characteristic with a peak at around 180 Hz and a high-frequency plateau, implying dependence on the magnitude of slit displacement (position) in addition to the resonant behavior around 180 Hz. The third PDM has a low-pass characteristic that implies dependence only on the integrated (cumulative) slit displacement/position over a 6 ms time-window. The magnitude of the first PDM is similar between the two neuron types (with the type B neuron exhibiting a greater initial slope below 180 Hz), but the magnitude of the other two PDMs tended to be larger for the Type B neurons.

For comparison purposes and in order to verify that the obtained dynamic characteristics were not affected by the output action potential data preprocessing, we also estimated the three PDMs from the raw output

data (middle panels of Fig. 2). Their frequency response characteristics were similar to those shown in Fig. 6, except that the peak of the second PDM was located at a slightly lower frequency (i.e., 150 Hz instead of 180 Hz) and the first PDM reached its plateau earlier (around 200 Hz, instead of around 350 Hz). Therefore, the subsequent analysis is based on the PDMs obtained from the processed (binary) output waveforms.

The results of the multiple linear regression analysis for the data segments used to estimate the Volterra kernels are summarized in Table 3, where we show the values of the regression coefficients, normalized by the RMS value of the corresponding input, for all four neurons. The achieved NMSEs for the regression model were equal to 92–93%, i.e., larger than their linear Volterra model counterparts—note that the regression model does not incorporate cumulative position information—and considerably larger than their nonlinear model counterparts, as expected due to the strong nonlinearities present in the system dynamics. The coefficient values imply stronger dependence on displacement position for all neurons, followed by displacement velocity and then acceleration for three out of four neurons. It is interesting to note that the inclusion of acceleration terms in the regression model improved the NMSEs by 1–1.5%, except in the case of one neuron (Type B, Neuron 2), for which the improvement was not significant (mean NMSEs 92.82 and 92.78%, respectively, $p > 0.15$ for eight out of ten data segments). This was reflected on the magnitude of the coefficients, since the acceleration coefficient for this neuron exhibited small magnitude values and was mostly positive, whereas for the rest of the neurons it was negative and exhibited larger magnitudes.

In order to illustrate the combinations of PDM output values that gave rise to action potentials at the mechanoreceptor output, we show three-dimensional scatter

Table 3 Multiple linear regression coefficients between mechanoreceptor displacement, displacement velocity and displacement acceleration (inputs) and action potential data (output), normalized by the corresponding input RMS values and averaged over ten 5 s data segments

	Type A		Type B	
	Neuron 1	Neuron 2	Neuron 1	Neuron 2
β_0	0.038 ± 0.001	0.054 ± 0.002	0.073 ± 0.003	0.069 ± 0.004
β_1	2.006 ± 0.052	2.354 ± 0.059	2.721 ± 0.084	3.435 ± 0.127
β_2	1.489 ± 0.058	2.010 ± 0.114	1.670 ± 0.180	2.475 ± 0.188
β_3	-0.920 ± 0.064	-1.377 ± 0.055	-1.876 ± 0.076	0.183 ± 0.077

Values are mean \pm SE

β_0 constant term, β_1 displacement term, β_2 velocity term, β_3 acceleration term

plots of the PDM output values that corresponded to action potentials (blue) along with those that did not (red) for the Type A and Type B neurons in Figs. 7 and 8, respectively, as well as their corresponding two-dimensional projections on the $\{u_1, u_2\}$ and $\{u_1, u_3\}$ planes in Figs. 9 and 10. The construction of the three-input nonlinear function $f(u_1, u_2, u_3)$ was based on these scatter plots through three-dimensional histogramming that yielded the “Probability of Firing Function” (PFF) for each neuron. The form of the scatter plots and their projections indicates that both neuron types exhibit

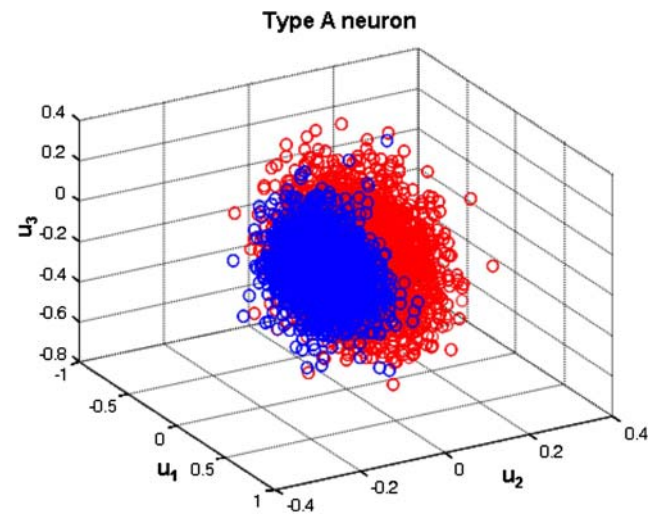


Fig. 7 Scatter plot of the PDM output values that correspond to action potentials (blue) for a Type A neuron. Note the strongly directional behavior with respect to the output of the second PDM (u_2), with action potentials corresponding only to negative u_2 values

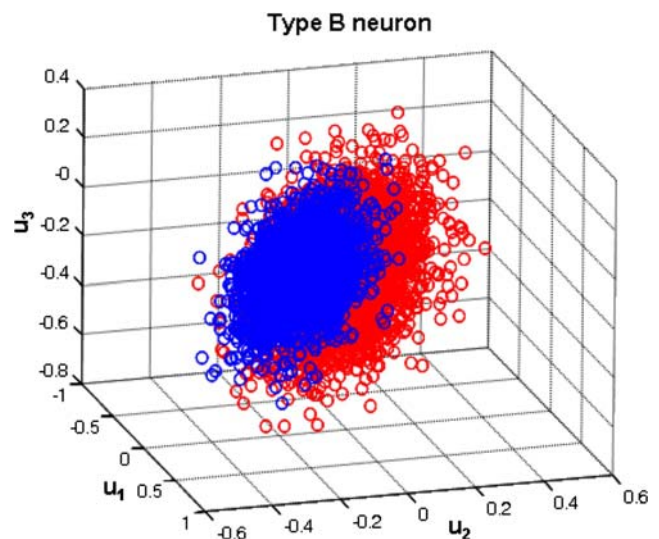


Fig. 8 Scatter plot of the three PDM output values that correspond to action potentials (blue) for a Type B neuron. Note the similarity to the mapping of Fig. 7 (Type A neuron)

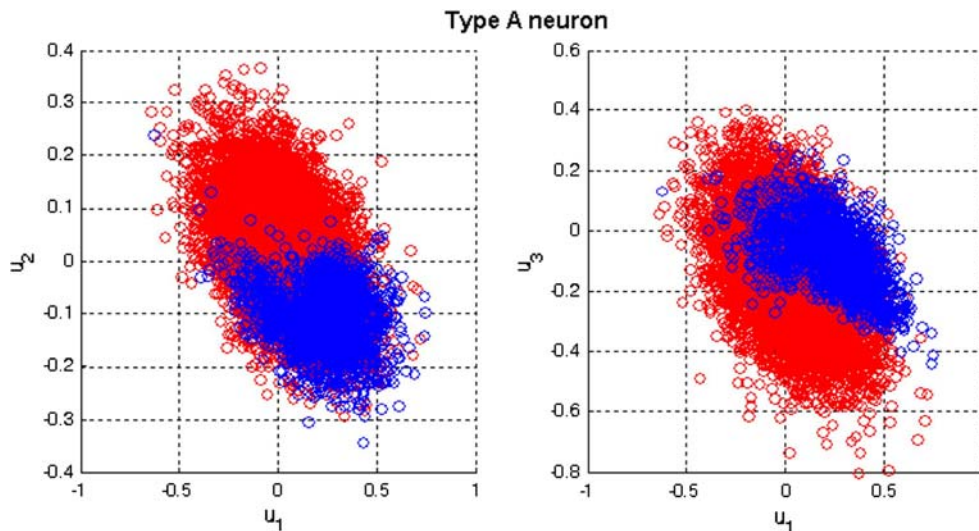


Fig. 9 Projection of the three-dimensional scatter plot of Fig. 7 on the $\{u_1, u_2\}$ and $\{u_1, u_3\}$ planes (*left and right panels*, respectively). Note the strongly directional dependence on u_2

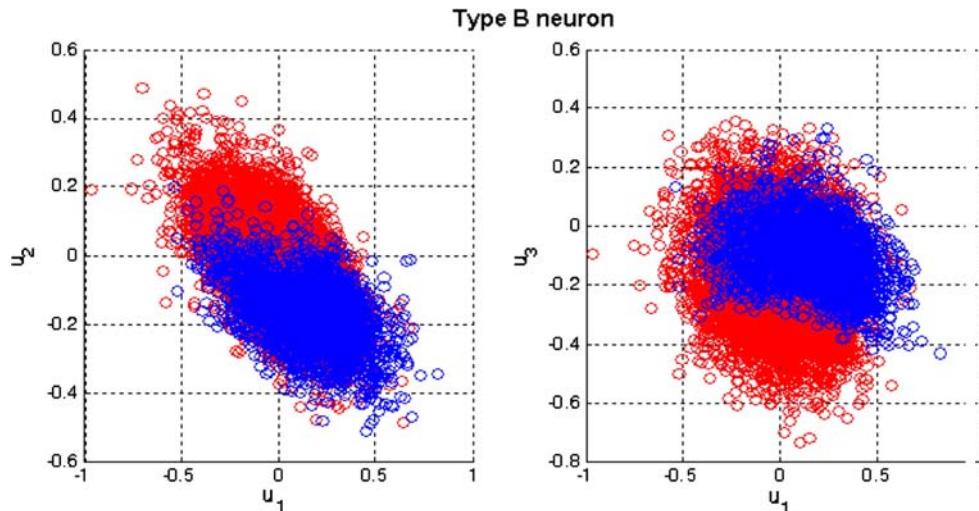


Fig. 10 Projection of the three-dimensional scatter plot of Fig. 8 on the $\{u_1, u_2\}$ and $\{u_1, u_3\}$ planes (*left and right panels*, respectively)

directionality with respect to the PDM output values (e.g., output action potentials corresponded to both positive and negative values of u_1, u_3 , but almost all the output action potentials corresponded to negative values of u_2).

Since $f(u_1, u_2, u_3)$ is three-dimensional, we plot its one-dimensional projections (marginal probabilities) on $\{u_i\} f_M(u_i)$, where $i = 1, 2, 3$, in Fig. 11 for one Type A and one Type B neuron. Their form is similar for the two neurons, in agreement to the observations made for the scatter plots. The first projection $f_M(u_1)$ is asymmetric with respect to the magnitude of u_1 around zero, exhibiting significantly larger values for increasing u_1 positive values, i.e., it depends on both direction and magnitude of the slit displacement velocity. The second

projection $f_M(u_2)$ is strongly asymmetric with respect to its argument, yielding significant values for negative u_2 values only and implying directional dependence on slit displacement position. On the other hand, the marginal probability $f_M(u_3)$ is symmetric around zero; therefore it depends only on the magnitude of the cumulative slit displacement over a short sliding window. Overall, the asymmetric behavior was more pronounced for the output of the band-pass PDM u_2 . Similar observations were made for the remaining two neurons as well.

The ROC curves for the in-sample data (i.e., the points that were used to compute the PFF) and for the validation (out-of-sample) data for a Type B neuron are shown in Fig. 12 for a histogramming bin size of 0.1. The ROC curves for the rest of the neurons were found

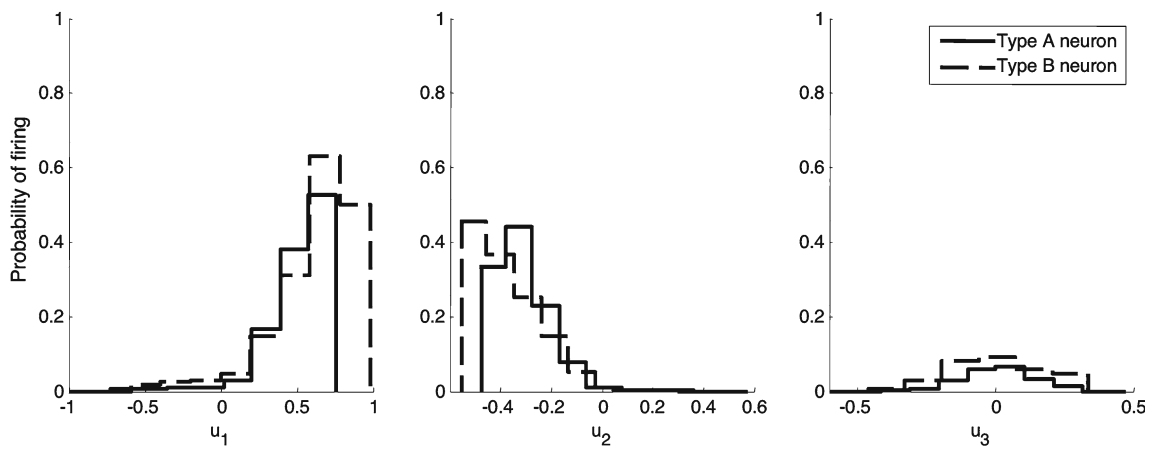


Fig. 11 Projections of the three-dimensional static nonlinearity on ($i = 1, 2, 3$; one-dimensional marginal probability functions) for one Type A and one Type B neuron. Note the strongly asymmetric dependence on u_1 and u_2 (outputs of velocity and position encoding PDMs) and the symmetric dependence on u_3 (output of cumulative position encoding PDM)

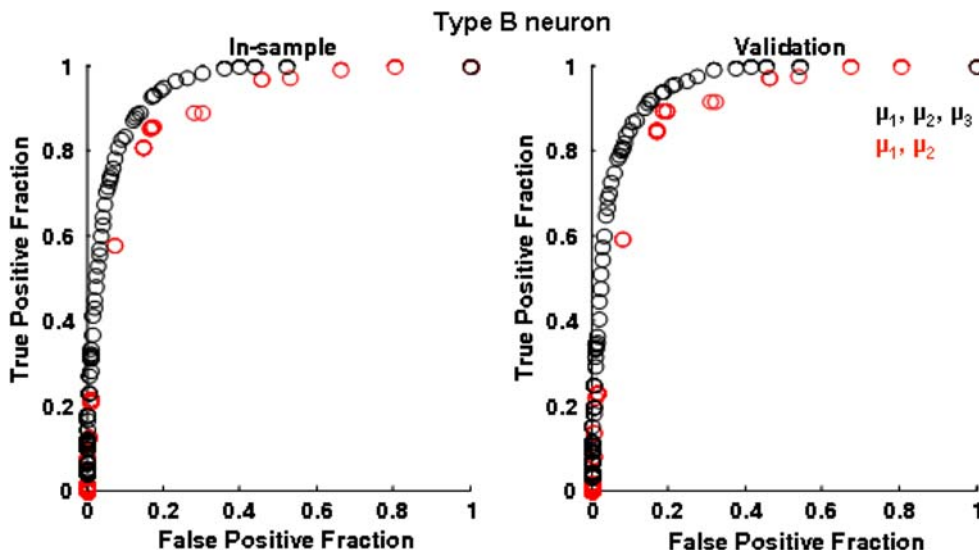


Fig. 12 ROC curves for a Type B neuron for two (red) and three (black) PDM models. The use of three PDMs improves the model performance considerably

to be similar to those of Fig. 12. When three PDMs were utilized (black), i.e., a three-dimensional PFF was constructed, the performance improved considerably compared to two PDMs (red), which yielded a two-dimensional PFF. The ROC curve is a suitable measure of model performance in terms of predicting output action potentials, since it yields an overall assessment of performance for all values of the threshold p , which can be quantified by calculating the area under the curve. The values of the area under the ROC curves of Fig. 12 were equal to 0.930/0.957 (in-sample data) and 0.938/0.960 (validation data) for two/three PDMs, respectively. The model performance for the validation data set is thus comparable to its in-sample counterpart, corroborating the validity of the modeling results.

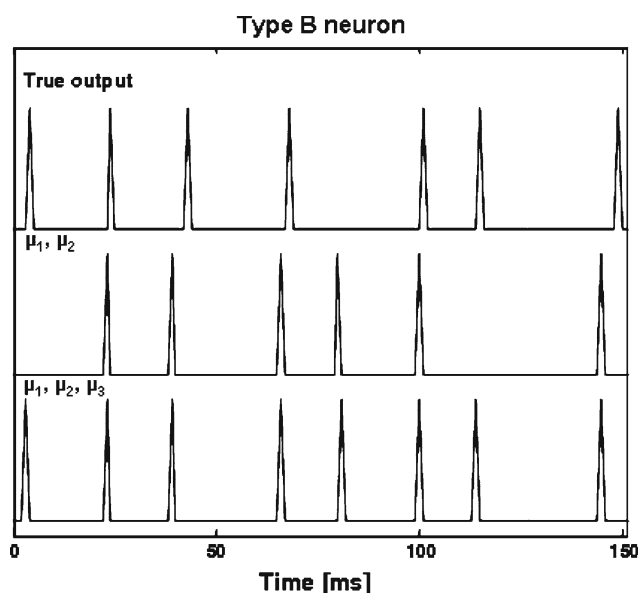
The corresponding values for all four neurons are given in Table 4 for three different histogramming bin sizes (0.02, 0.05 and 0.1). For smaller bin sizes (i.e., finer resolution in the PFF computation), the performance improved for the in-sample data but degrades considerably for the validation data (Table 4). This is to be expected, since the number of data points corresponding to action potentials was low compared to the total number of data points. Consequently, we did not have enough information in the data in order to increase the PFF resolution while, at the same time, maintaining the model generalization capability. The best overall performance for both in-sample and validation data was observed for a bin size of 0.1. For comparison purposes, the values of the area under the ROC curve achieved

Table 4 Area under the ROC curve for output action potential prediction for different histogramming bin sizes, Type A and B neurons

	Bin size	Type A		Type B	
		Neuron 1	Neuron 2	Neuron 1	Neuron 2
Linear					
In-sample	–	0.987	0.952	0.912	0.948
Validation	–	0.989	0.953	0.919	0.956
μ_1, μ_2					
In-sample	0.02	0.986	0.942	0.933	0.960
	0.05	0.986	0.939	0.938	0.964
	0.1	0.987	0.939	0.930	0.966
Validation	0.02	0.986	0.919	0.932	0.953
	0.05	0.987	0.933	0.941	0.958
	0.1	0.988	0.936	0.938	0.958
μ_1, μ_2, μ_3					
In-sample	0.02	0.995	0.987	0.975	0.974
	0.05	0.990	0.973	0.960	0.971
	0.1	0.989	0.971	0.957	0.973
Validation	0.02	0.945	0.890	0.910	0.853
	0.05	0.989	0.959	0.956	0.962
	0.1	0.989	0.969	0.960	0.965

by linear Volterra models are also given. Interestingly, nonlinear models improve the performance marginally for one Type A neuron, while this improvement is substantial for all other neurons, especially for the two Type B neurons. This suggests that the nonlinear component is stronger in the latter.

The action potential prediction achieved by the model is shown in Fig. 13 for a representative 150 ms validation

**Fig. 13** Representative output action potential prediction for a Type B neuron for two and three PDM models. The three PDM nonlinear model yields better performance

segment taken from a Type B neuron. The predicted output action potential traces shown here correspond to a threshold of 0.2. The number and location of output action potentials were predicted with accuracy, with the three-PDM model performing better.

4 Conclusions and discussion

The presented results demonstrate that the encoding of mechanical stimuli into action potentials in two types of mechanoreceptor neurons in a spider lyriform organ can be described by a nonlinear model that consists of three PDMs (linear filters) followed by a three-dimensional static nonlinearity and a threshold function. This model is able to predict the generated action potentials in response to broadband mechanical stimuli accurately, as quantified by the computed ROC curves (which measure the true-positive vs. false-positive performance of the model in predicting output spikes). The form of the three PDMs suggests that the dynamics of these mechanoreceptors exhibit high-pass, band-pass and low-pass characteristics. This implies that action potential generation in these mechanoreceptors depends on both position and velocity of the slit displacement, as well as on the cumulative displacement over a short sliding window. The effect of the displacement velocity appears to be dominant. Moreover, the form of the static nonlinearity reveals that the generation of action potentials is directionally selective, mainly with respect to the output of the second (band-pass) PDM, for which it exhibits half-wave rectification characteristics.

The dynamics of the two neuron types were generally similar, although some differences were observed in the magnitude of the second (band-pass) and third (low-pass) PDMs, which were found to be larger for Type B neurons. Differences were also observed in the frequency-domain slope of the first (high-pass) PDM below 180 Hz, which may be significant for the overall response characteristics of the neuron, since most of the mechanical stimulus power was below 180 Hz. The constant component of the model (zeroth-order kernel), which is related to the average firing rate, was also found to be considerably larger for Type B neurons. These observations extend our previous modeling studies of the transduction of mechanical stimuli into intracellular receptor current and voltage (Marmarelis et al. 1999) and parallel cascade modeling of the encoding of mechanical stimuli into action potentials (French et al. 2001).

The Volterra–Wiener approach has been employed widely for modeling physiological systems (Marmarelis 2004). It is well-suited to the complexity of such systems,

since it yields rigorous mathematical descriptions of their dynamic behavior by utilizing input–output data, without requiring any a priori assumptions about system structure. In the case of sensory systems, Volterra–Wiener models have been employed extensively in the visual (Sakai 1992) and auditory systems (Eggermont 1993), in addition to the study of mechanoreceptor function. The general Volterra model of Eq. (1) can be viewed as a generalization of the convolution operation, which describes the dynamic input–output relationship for linear systems, to nonlinear systems. The first-order (linear) Volterra kernel describes the linear effects of the system input on the output, and the Q th order ($Q > 1$) nonlinear kernel describes the effect of the interaction of Q past values of the input on the present value of the system output. Note that the first-order (linear) Volterra kernel is *not* equivalent to the system impulse response in this case, since the impulse response of a Volterra system depends not only on the first-order kernel, but on the diagonal points of the higher-order kernels as well.

Nonlinear models were found to improve the model performance considerably, when compared to linear models, in terms of both prediction NMSE (10–15% reduction) and area under the ROC curve (Table 4). As shown in Fig. 5, the third-order Volterra functional terms further improved the output prediction of second-order models by building on the spike locations without inserting new false spike locations, thus increasing the prediction SNR and resulting in about 5% reduction of the prediction NMSE (from around 80 to 75%). However, second and third-order models yielded comparable ROC curve area values. This may be attributed to the fact that third-order models built mainly on the contribution of second-order models to both true and false positive spikes, without altering significantly the relation between true and false positives. The improvement observed for nonlinear models was more pronounced for Type B neurons, implying a stronger nonlinear component in the dynamics of the latter. This is corroborated by the increase in the area under the ROC curve, which was larger for Type B neurons than Type A neurons and is in agreement with the observation that the magnitudes of the second and third PDMs, μ_2 and μ_3 , which reside mainly in the nonlinear dynamics, were larger for the Type B neurons. Interestingly, linear models performed better than the two-mode nonlinear models in the case of Type A neurons (Table 4), due to the fact that the nonlinear component was weaker in these neurons and also to that the third PDM of Type A neurons was found to explain a larger fraction of the system dynamics. The latter was concluded by expressing the first-order kernel as a linear combination of the first two PDMs for both neuron types, whereby it was found

that the corresponding NMSE was considerably larger for Type A neurons (representative values: 30% and 3% for Type A and B neurons, respectively). In other words, the third PDM was more linearly independent to the first two PDMs in the case of Type A neurons. The presence of third-order nonlinearities in the mechanoreceptor function is also suggested by the form of the calculated two-dimensional PFFs (not shown here), which exhibited half-wave rectification characteristics.

The characteristics of the three PDMs suggest that both Type A and B neurons are able to encode more than one parameter of the slit displacement stimulus (i.e., velocity, position and cumulative position). The first PDM, which resembled the first-order Volterra kernel, had a differentiating (high-pass) characteristic and encoded primarily the stimulus velocity—although some position encoding also took place by virtue of the fact that the positive and negative peak deflections of the PDM in the time domain were not equal (they would be equal in case of a strictly differentiating PDM). The second and third PDMs had mixed band-pass and low-pass characteristics, implying encoding of velocity (within a preferred range defined by the pass-band), position and cumulative position. The strong dependence of mechanoreceptor encoding on displacement position and velocity was also confirmed by the results of the linear regression analysis (Table 3). The regression coefficient corresponding to position exhibited the largest magnitude for all four neurons, followed by the velocity coefficient for three out of four neurons. Moreover, the incorporation of acceleration terms in the regression model was found to improve the regression NMSEs in three out of four neurons, implying that acceleration encoding is also taking place. Note, however, that the regression model does not take into account dynamic information such as cumulative position, which was found to have a considerable effect; hence the achieved performance is worse in terms of predicting the mechanoreceptor output.

The obtained PDMs bear similarities to their counterparts estimated from transmembrane receptor and current recordings from spider mechanoreceptors (Marmarelis et al. 1999). However, in that previous study, two significant PDMs were identified, with the first having a low-pass characteristic (that was more pronounced for potential than for current measurements) and the second having a high-pass characteristic but residing mainly in the nonlinear dynamics. On the other hand, the two PDMs estimated from action potential encoding in a cockroach tactile spine neuron were less similar and exhibited all-pass (i.e., position dependent) and band-pass (with a resonant peak around 20 Hz) characteristics, respectively (French and Marmarelis 1995).

The presence of position, position-velocity, pure velocity and acceleration dependent afferents has been also reported for proprioceptors in crab (Gamble and DiCaprio 2003) and locust chordotonal organs (Kondoh et al. 1995), where in addition the presence of mixed velocity–acceleration sensitive afferents was reported.

The scatterograms of Figs. 7, 8, 9, 10 show that the mapping between the PDM output values and the resulting action potentials was similar in Type A and B neurons, which is also reflected in the PFFs of Fig. 11. The latter suggest that action potential encoding was directionally selective mostly with respect to the preferred-velocity and position of the displacement, since the marginal PFF $f_M(u_2)$ was nonzero for negative values of the second PDM output u_2 only (Fig. 11, middle panel). Moreover, asymmetric dependence with respect to the primarily velocity-dependent PDM output u_1 (Fig. 11, left panel), as well as symmetric dependence on the cumulative position PDM output u_3 (Fig. 11, right panel), were also observed. The strong directional selectivity with respect to position was also observed for the transduction of mechanical stimuli into transmembrane current and potential (Marmarelis et al. 1999).

The lack of strong differences between the dynamics of Type A and B neurons has been reported previously for parallel cascade estimates of linear and nonlinear Volterra kernels (French et al. 2001). The discrepancy observed between their estimated zeroth-order kernel values may reflect their differences in the recovery from Na^+ channel inactivation. Voltage-activated sodium current (I_{Na}) is primarily responsible for the leading edge of the action potential in many neurons. While I_{Na} generally activates rapidly when a neuron is depolarized, its inactivation properties vary significantly among different neurons and it can occasionally exhibit slowly and rapidly inactivating components within the same neuron. In the case of Type A and B neurons, it has been shown with voltage-clamp experiments (Torkkeli et al. 2001) that the differences in their response characteristics are due primarily to the Na^+ channel inactivation properties and particularly the recovery from inactivation, which was found to be significantly slower in Type A neurons. The same was demonstrated by using a simplified Hodgkin–Huxley model (Torkkeli and French 2002), where the firing patterns of Type A and B neurons were reproduced by using different time constants for the I_{Na} recovery from inactivation (120 and 40 ms, respectively), as well as different slope factors (5 and 9 mV, respectively). However, the fast I_{Na} activation and inactivation dynamics, which have been shown to be similar in Type A and B neurons with single time constants of 2–3 and 5–10 ms, respectively (Torkkeli

et al. 2001), may dominate the obtained estimates in the present study (the kernel memory was found to be about 10–15 ms). Therefore, we postulate that the different characteristics of the I_{Na} recovery from inactivation are reflected mainly on the zeroth-order model component. We must also note that pseudorandom stimulation results in continuous action potential firing, therefore Na^+ channels may not be inactivated or recover from inactivation completely, as in the case of step stimulation used in the aforementioned studies.

In conclusion, the PDM analysis provides a compact representation of mechanoreceptor dynamics, which describes quantitatively their ability to encode multiple features of mechanical stimuli and achieves excellent performance in terms of predicting the resulting action potentials. It can also assist in understanding and dissecting the underlying physiological mechanisms, when combined with suitable experimental manipulation of the relevant ionic processes.

References

- Bose AG (1956) A theory of nonlinear systems. Technical Report No. 309. Research Laboratory of Electronics, MIT, Cambridge
- Del Prete Z, Baker SP, Grigg P (2003) Stretch responses of cutaneous RA afferent neurons in mouse hairy skin. *J Neurophysiol* 89:1649–1659
- DiCaprio RA (2003) Nonspiking and spiking proprioceptors in the crab: nonlinear analysis of nonspiking TCMRO afferents. *J Neurophysiol* 89:1826–1836
- Egan JP (1975) Signal detection theory and ROC analysis. Academic, New York
- Eggermont JJ (1993) Wiener and Volterra analyses applied to the auditory system. *Hear Res* 66:177–201
- Finkel AS, Redman S (1984) Theory and operation of single microelectrode voltage clamp. *J Neurosci Meth* 11:101–127
- French AS (1992) Mechanotransduction. *Annu Rev Physiol* 54:135–152
- French AS, Holden AV (1971) Alias-free sampling of neuronal spike trains. *Kybernetik* 8:165–171
- French AS, Holden AV, Stein RB (1972) The estimation of the frequency response function of a mechanoreceptor. *Kybernetik* 11:15–23
- French AS, Korenberg MJ (1989) A nonlinear cascade model for action potential encoding in an insect sensory neuron. *Biophys J* 55:655–661
- French AS, Patrick SK (1994) A nonlinear model of step responses in the cockroach tactile spine neuron. *Biol Cybern* 70:435–441
- French AS, Marmarelis VZ (1995) Nonlinear neuronal mode analysis of action potential encoding in the cockroach tactile spine neuron. *Biol Cybern* 73:425–430
- French AS, Höger U, Sekizawa S-i, Torkkeli PH (2001) Frequency response functions and information capacities of paired mechanoreceptor neurons. *Biol Cybern* 85:293–300
- Gamble ER, DiCaprio RA (2003) Nonspiking and spiking proprioceptors in the crab: white noise analysis of spiking CB-chordotonal organ afferents. *J Neurophysiol* 89:1815–1825
- Juusola M, French AS (1995) Transduction and adaptation in spider slit sense organ mechanoreceptors. *J Neurophysiol* 74:2513–2523

- Juusola M, Weckström M, Uusitalo RO, Korenberg MJ, French AS (1995) Nonlinear models of the first synapse in the light-adapted fly retina. *J Neurophysiol* 74:2538–2547
- Juusola M, Seyfarth EA, French AS (1997) Rapid coating of glass-capillary microelectrodes for single-electrode voltage clamp. *J Neurosci Meth* 71:199–204
- Koles ZJ, Smith RS (1974) Characteristics of the sensory discharge of the muscle spindle in *Xenopus laevis*. *Kybernetik* 15:99–110
- Kondoh Y, Okuma J, Newland PL (1995) Dynamics of neurons controlling movements of a locust hind leg: Wiener kernel analysis of the responses of proprioceptive afferents. *J Neurophysiol* 73:1829–1842
- Looft PJ, Baltensperger CM (1990) Linear systems analysis of cutaneous type I mechanoreceptors. *IEEE Trans Biomed Eng* 37:565–573
- Marmarelis VZ (1989) Signal transformation and coding in neural systems. *IEEE Trans Biomed Engin* 36:15–24
- Marmarelis VZ (1993) Identification of nonlinear biological systems using Laguerre expansion of kernels. *Ann Biomed Eng* 21:573–589
- Marmarelis VZ (1997) Modeling methodology for nonlinear physiological systems. *Ann Biomed Eng* 25:239–251
- Marmarelis VZ (2004) Nonlinear dynamic modeling of physiological systems. IEEE Press & Wiley-Interscience, Hoboken, New Jersey
- Marmarelis VZ, Juusola M, French AS (1999) Principal dynamic mode analysis of nonlinear transduction in a spider mechanoreceptor. *Ann Biomed Eng* 27:391–402
- Marmarelis VZ, Orme ME (1993) Modeling of neural systems by use of neuronal modes. *IEEE Trans Biomed Engin* 40:1149–1158
- Matthews PC, Stein, RB (1969) The sensitivity of muscle spindle afferents to small sinusoidal changes in length. *J Physiol (Lond)* 200:723–743
- McFall RM, Treat, TA (1999) Quantifying the information value of clinical assessments with signal detection theory. *Annu Rev Psychol* 1999:50215–50241
- Sakai HM (1992) White-noise analysis in neurophysiology. *Phys Rev* 72:491–505
- Sekizawa S-i, French AS, Höger U, Torkkeli PH (1999) Voltage-activated potassium outward currents in two types of spider mechanoreceptor neurons. *J Neurophysiol* 81:2937–2944
- Seyfarth EA, French AS (1994) Intracellular characterization of identified sensory cells in a new spider mechanoreceptor preparation. *J Neurophysiol* 71:1422–1427
- Swets JA, Pickett RM (1992) Evaluation of diagnostic systems: Methods from signal detection theory. Academic, New York
- Torkkeli PH, Sekizawa S-i, French AS (2001) Inactivation of voltage-activated Na^+ currents contributes to different adaptation properties of paired mechanosensory neurons. *J Neurophysiol* 85:1595–1602
- Torkkeli PH, French AS (2002) Simulation of different firing patterns in paired spider mechanoreceptor neurons: The role of Na^+ channel inactivation. *J Neurophysiol* 87:1363–1368
- Webber RM, Stanley GB (2004) Nonlinear encoding of tactile patterns in the barrel cortex. *J Neurophysiol* 91:2010–2022